

PAPER • OPEN ACCESS

## Covert-inspired flaps: an experimental study to understand the interactions between upperwing and underwing covert feathers

To cite this article: Diaa A Zekry *et al* 2023 *Bioinspir. Biomim.* **18** 046021

View the [article online](#) for updates and enhancements.

### You may also like

- [Influence of P300 latency jitter on event related potential-based brain–computer interface performance](#)  
P Aricò, F Aloise, F Schettini *et al.*
- [Feather-inspired flow control device across flight regimes](#)  
Ahmed K Othman, Nirmal J Nair, Andres Goza *et al.*
- [Imagined speech increases the hemodynamic response and functional connectivity of the dorsal motor cortex](#)  
Xiaopeng Si, Sicheng Li, Shaoxin Xiang *et al.*

# Bioinspiration & Biomimetics



## PAPER

# Covert-inspired flaps: an experimental study to understand the interactions between upperwing and underwing covert feathers

### OPEN ACCESS

RECEIVED  
5 March 2023

REVISED  
10 May 2023

ACCEPTED FOR PUBLICATION  
1 June 2023

PUBLISHED  
27 June 2023

Diaa A Zekry<sup>1</sup> , Taewoo Nam<sup>2</sup>, Rikin Gupta<sup>2</sup>, Yufei Zhu<sup>2</sup> and Aimy A Wissa<sup>1,\*</sup> 

<sup>1</sup> Princeton University, Princeton, NJ 08544, United States of America

<sup>2</sup> Toyota Motor Engineering and Manufacturing North America, Inc., Ann Arbor, MI 48103, United States of America

\* Author to whom any correspondence should be addressed.

E-mail: [awissa@princeton.edu](mailto:awissa@princeton.edu)

**Keywords:** covert-inspired flaps, bio-inspired flight control, feather-inspired flaps

Original Content from  
this work may be used  
under the terms of the  
[Creative Commons  
Attribution 4.0 licence](https://creativecommons.org/licenses/by/4.0/).

Any further distribution  
of this work must  
maintain attribution to  
the author(s) and the title  
of the work, journal  
citation and DOI.



## Abstract

Birds are agile flyers that can maintain flight at high angles of attack (AoA). Such maneuverability is partially enabled by the articulation of wing feathers. Coverts are one of the feather systems that has been observed to deploy simultaneously on both the upper and lower wing sides during flight. This study uses a feather-inspired flap system to investigate the effect of upper and lower side coverts on the aerodynamic forces and moments, as well as examine the interactions between both types of flaps. Results from wind tunnel experiments show that the covert-inspired flaps can modulate lift, drag, and pitching moment. Moreover, simultaneously deflecting covert-inspired flaps on the upper and lower sides of the airfoil exhibit larger force and moment modulation ranges compared to a single-sided flap alone. Data-driven models indicate significant interactions between the upper and lower side flaps, especially during the pre-stall regime for the lift and drag response. The findings from this study are also biologically relevant to the observations of covert feathers deployment during bird flight. Thus, the methods and results summarized here can be used to formulate new hypotheses about the coverts role in bird flight and develop a framework to design covert-inspired flow and flight control devices for engineered vehicles.

## 1. Introduction

Birds like the bald eagle and the goshawk are known for their ability to repeatedly perform high angle of attack (AoA) maneuvers like takeoff, landing, and perching. These birds and others commonly use a combination of wing articulation [1] and tail articulation [2–4] to achieve such maneuverability. Wing articulation methods consist of large-scale shape morphing [1], such as changes in sweep and dihedral, and small-scale shape changes [5], such as feather deflections. Recent work has focused on explaining how large-scale shape changes affect birds' maneuverability [6]. However, small-scale shape changes can also effectively modulate aerodynamic forces and moments during flight. Covert feathers deployment is one example of a small-scale shape change that has been observed to play a significant role during flight [5].

Coverts are contour feathers that cover most of the upper side and the thick leading edge part of the

lower side. Rows of covert feathers start near the leading edge and extend toward the trailing edge. Thus, they are affected by both the pressure suction peak at the leading edge and the separated flow near the trailing edge. Figure 1 shows the main anatomical divisions of the coverts on both the upper and lower sides of the birds' wings. Coverts are divided into primary coverts and secondary feathers coverts, covering the hand wing and the arm wing, respectively. Secondary coverts are further divided into lesser, median, and greater, moving from the leading edge to the trailing edge [5, 7, 8]. Flight observations show that coverts deploy passively in response to pressure changes on the wing's surfaces during maneuvers and sudden changes in the flow conditions. A study by Carruthers *et al* [5] recorded the deployment of the coverts feathers on steppe eagles *Aquila nipalensis* during flight maneuvers. The authors reported, through video recordings, that the upperwing and underwing coverts are usually observed to deploy simultaneously. Specifically, they reported the following observations



(OBS) during landing and glide perching maneuvers [5]:

- OBS 1: lesser underwing coverts deployed in most landing and perching maneuvers.
- OBS 2: underwing coverts deployment was often accompanied by upperwing coverts deployment and alula, another group of feathers, protraction.
- OBS 3: greater upperwing coverts deployed during gust encounters.
- OBS 4: lesser underwing coverts deployed towards the end of the pitch-up phase of the perch maneuver.

Observations of covert feathers during bird flight have inspired the design of covert-inspired flow control devices. Researchers showed that suction, or upperwing, covert-inspired flaps increase post-stall lift by enabling the suction side to maintain lower pressure through the pressure dam effect. Further, covert-inspired flaps decrease separation propagation on the upper surface, improving the wing resistance to stall [9–18]. However, despite the number of engineering studies on covert-inspired flaps and bird flight observations indicating that the coverts in nature deploy simultaneously on the upper and under wings [5], prior work mainly studied the suction (upper) side coverts deflected alone [9, 10] or the pressure (lower) side, coverts deflected alone [16]. No studies have investigated the effects of simultaneous deflection of pressure and suction side coverts on aerodynamic performance, nor have they examined the significance of the interaction between them.

Thus, in this study, we seek to answer the following questions:

**Q1** What is the effect of simultaneous static deflection of pressure and suction covert-inspired flaps

on the aerodynamic forces and moments compared to a single-sided flap alone?

**Q2** Which flap parameters are most effective at modulating the aerodynamic forces and moments?

**Q3** What are the interactions between the suction and pressure side covert-inspired flaps, are the flap effects purely additive, or do interactions between both flaps govern the aerodynamic response?

The remainder of the paper is divided into two sections: the aerodynamic characterization section and the data-driven modeling section. The aerodynamic characterization section answers the first and second questions. The data-driven modeling section further quantifies the answer for the second question by deriving mathematical models that relate the flap design parameters to the aerodynamic forces and moments and indicate the level of interaction between pressure and suction side flaps thus, answering the third question. The answers to the questions above can provide insights into the observations of covert deployment during bird flight. They can also enable novel covert-inspired flow and flight control devices for small-scale engineered vehicles to enhance maneuverability and aerodynamic efficiency. As an example, we conclude the paper with a case study for coverts as yaw control devices.

## 2. Aerodynamic characterization

### 2.1. Experimental methods

#### 2.1.1. Experimental setup

Experiments were conducted in an open-loop closed test section wind tunnel at the University of Illinois at Urbana Champaign (figure 2(a)). The wind tunnel is a low-speed tunnel with four test sections, each measuring 0.45 m in height, 0.9 m in width, and 1 m in length. The experiment was conducted

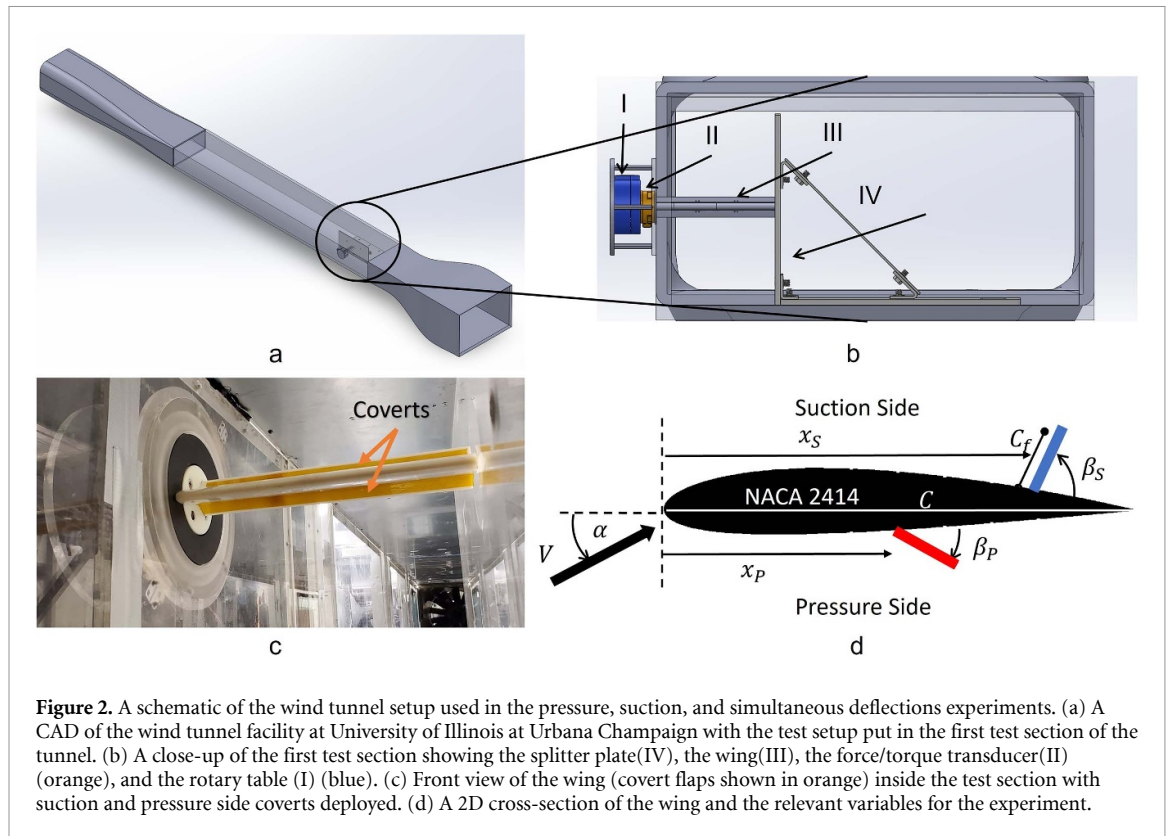


**Figure 2.** A schematic of the wind tunnel setup used in the pressure, suction, and simultaneous deflections experiments. (a) A CAD of the wind tunnel facility at University of Illinois at Urbana Champaign with the test setup put in the first test section of the tunnel. (b) A close-up of the first test section showing the splitter plate(IV), the wing(III), the force/torque transducer(II) (orange), and the rotary table (I) (blue). (c) Front view of the wing (covert flaps shown in orange) inside the test section with suction and pressure side coverts deployed. (d) A 2D cross-section of the wing and the relevant variables for the experiment.

in the first test section to minimize turbulence and boundary layer effects. We used a splitter plate to approximate the 2D flow (infinite airfoil) assumption (figure 2(b)) [19]. The wing section was connected to the splitter plate on one end with a paper-thin gap to avoid unintended reaction forces. On the other end, the wing was connected to an ATI Gamma six-axis force-torque transducer to measure the aerodynamic forces and moments on the wing. A Velmex stepper motor, shown in figure 2(b) (blue), controlled the airfoil pitch, effectively changing the angle of attack. The forces and moments measured from the transducer were transformed into the wind reference frame and non-dimensionalized into the conventional aerodynamic coefficients [20]. During the experiments, the free stream velocity was set to  $26 \text{ m s}^{-1}$ , corresponding to a Reynolds number of 200,000. Blockages were accounted for using solid and wake blockage equations [19].

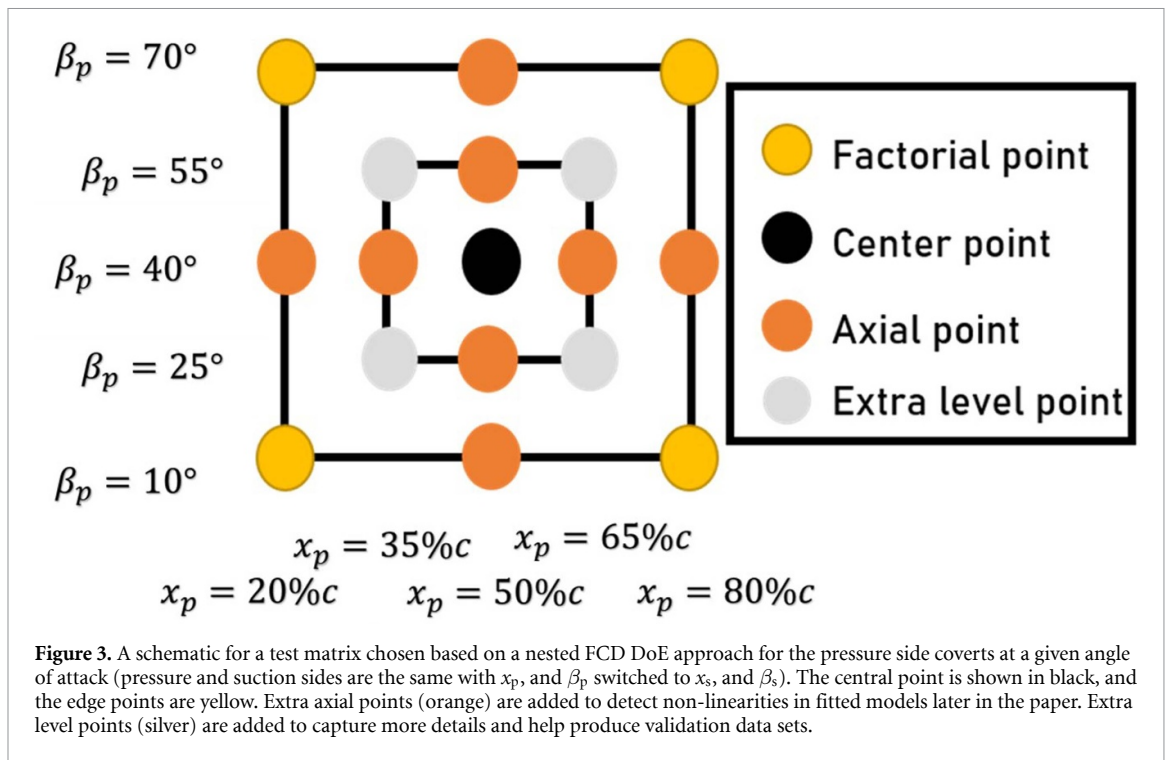
The airfoil was 3D printed using rigid 10 K material on an SLA Form 3 printer (figure 2(c)). It had a rectangular planform with a chord,  $c = 0.120 \text{ m}$ , and a span,  $b = 0.280 \text{ m}$ . The airfoil cross-section was a NACA 2414 profile, which was previously studied with covert-inspired flaps by [9, 21]. A schematic of the airfoil with the pressure and suction covert-inspired flaps is shown in figure 2(d). The flaps had a rectangular cross-section, and a chord length,  $c_f = 15\%c$ . The flaps spanned the entire airfoil, and a 3D-printed wedge was used to set the flap's deflection

angle. The deflection angle of the flaps remained static for a given test to examine the effect of the flap deployment angle on the aerodynamic forces and moments.

During the experiments, five parameters were varied, namely, the airfoil angle of attack (AoA),  $\alpha$ , the chord-wise location of the pressure side and suction side covert-inspired flaps,  $x_p$  and  $x_s$ , and the deflection angles of the pressure and suction side flaps,  $\beta_p$  and  $\beta_s$  (figure 2(d)). We conducted three sets of experiments: suction side only, pressure side only, and two-sided flap experiments. For the pressure side only experiments, the suction side flap was completely removed, and vice versa for the suction side experiments. The pressure side only and suction side only experiments are referred to as one-sided experiments, while the simultaneous pressure and suction sides experiments are referred to as double sided or two-sided experiments.

### 2.1.2. Design of experiments

A design of experiments (DoE) approach was used to determine the test matrix instead of the one factor at a time approach. DoE allows for a better scan of the design space in a limited-time facility like the wind tunnel [22, 23]. The DoE approach used in this paper was chosen such that it satisfies randomization and repetition. Randomization was satisfied through the random order in which the configurations were run. Repetition was applied by repeating



selected points more than three times to ensure that the averages had less than 5% variation between the readings. Also, since the experiments were conducted relatively quickly, blocking was unnecessary.

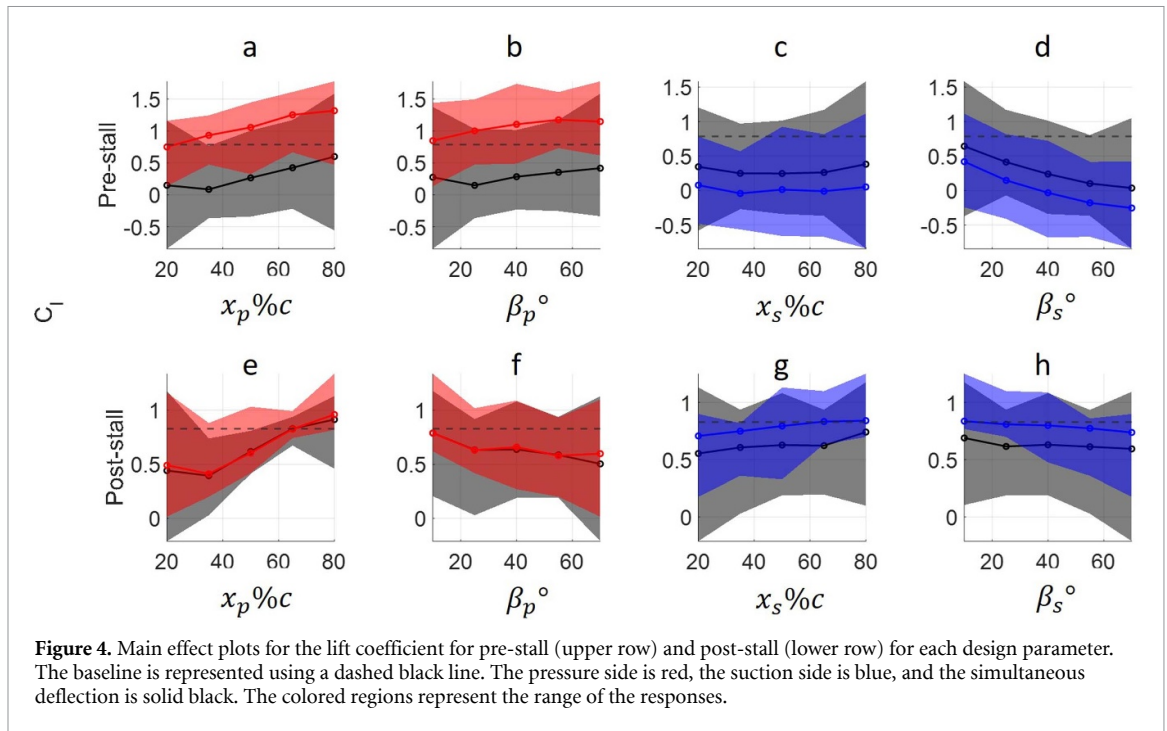
We used a nested face centered design (FCD) DoE for the one-sided and double-sided covert-inspired flap experiments. Nested FCD has been previously applied and validated for wind tunnel experiments [24, 25]. It can capture the non-linear behavior of the response with changing parameters using the extra level points. It also avoids over-fitting a model to a smaller number of points in a conventional factorial design. Figure 3 shows the nested FCD used to determine the test matrix for the pressure side covert-inspired flaps. The limits of the parameter space were defined by the boundary points (yellow). Then a central point was added to detect non-linearity (black). Since the aerodynamic responses are mostly nonlinear, we added axial points (orange) and extra level points (silver) to improve the model quality. The test matrix for the one-sided experiments was the same, with a change in parameter from  $x_p$  and  $\beta_p$  for the pressure side to  $x_s$  and  $\beta_s$  for the suction side. For the one-side experiments, the limits of the covert-inspired flap location were 20% $c$  and 80% $c$ , and the deflection angle limits were 10°–70°. For each flap configuration, the wing was swept through  $\alpha = -10^\circ$  to  $\alpha = 30^\circ$ . For the double-sided experiment, a four-dimensional nested FCD was used to determine the needed configurations covering the edge, central, and axial points. Then, second-level points were added to explore non-linearities and validate the derived

models. The location and deflection angle limits were the same as the one-side experiments.

## 2.2. Results

The results from the wind tunnel experiments are used to identify the effects of deploying the covert-inspired flaps on one side compared to simultaneously deploying them on the suction and pressure sides (Q1). More specifically, main effect plots are used to compare the effects of simultaneously deflecting pressure and suction sides covert-inspired flaps to deflecting a flap on one side only. The main effects plot shows a response's change to an input parameter while all other inputs are averaged. The responses considered here are lift, drag, and pitching moment, shown in figures 4 through 6, respectively, while the input parameters are  $x_p$ ,  $\beta_p$ ,  $x_s$ , and  $\beta_s$ . Each subplot has either a red line and shaded area for the pressure side flap only experiment or a blue line and shaded area representing the results for the suction side flap only experiment. The two-sided experiment results are shown using a black line and a grey shaded area in each subplot. The lines in the figures indicate the average, while the shaded regions represent the responses' range. Main effect plots are useful because they indicate the sensitivity of the response to each input parameter. For example, the positive slope of the black line in figure 4(a) indicates that pre-stall lift is sensitive to  $x_p$ , while the nearly zero slope in figure 4(c) indicates that pre-stall lift is not sensitive to  $x_s$ . Thus, in this case,  $x_p$  is more effective in modulating lift compared to  $x_s$ . For each of the responses considered,





the main effects are plotted for two flight regimes, namely pre-stall and post-stall. Each subplot, within figures 4 through 6, has a dashed grey line to represent the baseline experiment (i.e. the airfoil without any covert-inspired flaps).

### 2.2.1. Lift

First, we examine the main effects of the pressure side flap design parameters on lift. At pre-stall angles of attack, figures 4(a) and (b), moving the pressure side covert-inspired flap toward the trailing edge and increasing its deflection angle leads to an average increase in lift compared to the baseline. Thus, in pre-stall conditions, a pressure side covert-inspired flap deployed near the trailing edge acts similar to a traditional trailing edge flap. Post-stall lift is more sensitive to the location  $x_p$  than the deflection angle  $\beta_p$ , as indicated by the steeper slope of figure 4(e) compared to figure 4(f). However, at post-stall, a pressure side flap reduces lift on average compared to the baseline. The maximum and minimum values of attainable lift heavily depend on the flap's location and deflection angle at pre- and post-stall angles of attack (red shaded area in figures 4(a), (b), (e) and (f)).

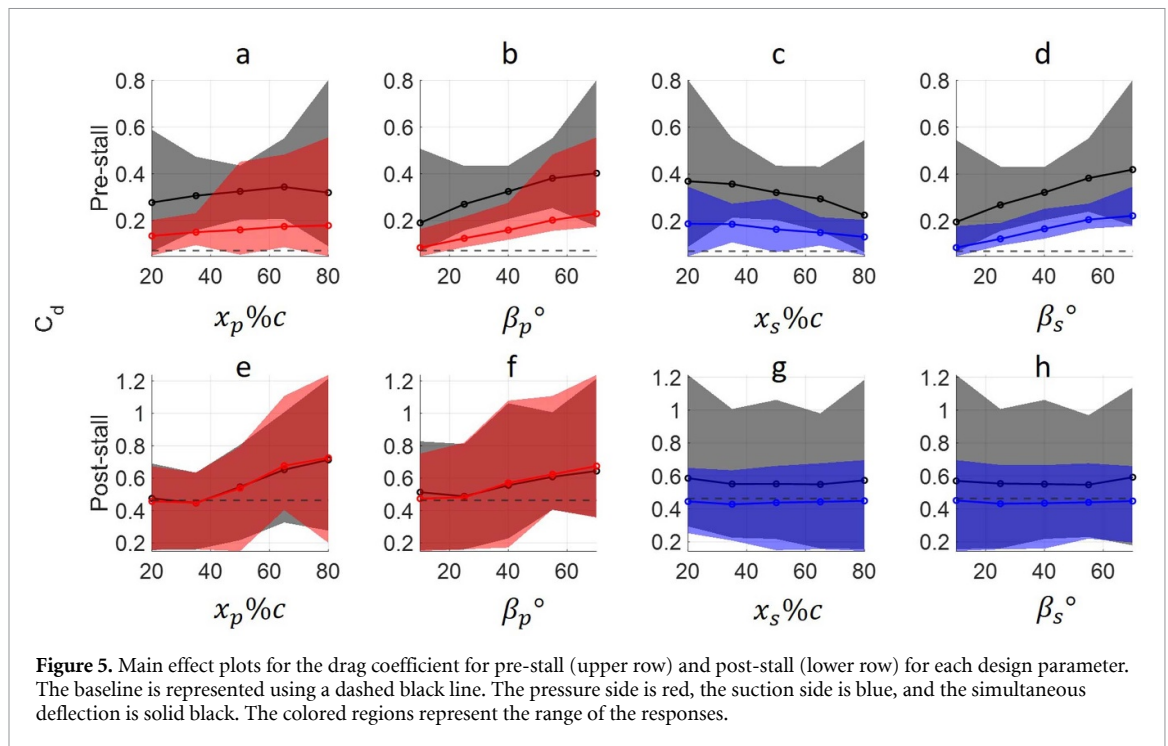
As for the suction side flap, at pre-stall (figures 4(c) and (d)), the lift is reduced compared to the baseline. On average, the location parameter,  $x_s$ , cannot modulate lift as much as the deflection angle,  $\beta_s$ , as indicated by the slopes of figures 4(c) and (d). The post-stall lift results for the suction side flap (figures 4(g) and (h)) show that, on average, the lift is insensitive to both  $\beta_s$  and  $x_s$ . However, the response ranges show that specific configurations can improve or reduce lift compared to the baseline. For

example, most post-stall lift improvement happens at the trailing edge flap location (i.e.  $x_s \geq 65\%$ ), which is consistent with the literature [14, 26].

The average simultaneous deflection results (figure 4, solid black lines) show that pre-stall lift is most sensitive to changes in the pressure side location,  $x_p$ , and suction side deflection angle,  $\beta_s$ . Increasing the latter decreases lift, and moving the former toward the trailing edge increases lift. It can also be seen from the zero slopes in figure 4 that the pre-stall lift is insensitive to the pressure side deflection angle,  $\beta_p$ , and the suction side location,  $x_s$ . As for the post-stall lift, it is mainly the pressure side location,  $x_p$ , that controls the lift response. As  $x_p$  moves from the leading edge to the trailing edge, the covert-inspired flap becomes more effective at increasing lift. For both regimes, the shaded grey regions show that for any given parameter, there is a combination of parameters that can enhance, reduce, or maintain lift compared to the baseline. The range between the minimum and maximum lift values is broad near both the leading and trailing edges and narrow at intermediate locations. Finally, compared to the one-sided experiments, the grey shaded region is wider than the red or blue alone. This result shows the advantages of the double sided or simultaneous deflection of both suction and pressure side covert-inspired flaps; deflecting both flaps together allows for a wider range of response modulation.

### 2.2.2. Drag

Drag is the second response considered for the one- and two-sided covert-inspired flaps experiments. We first examine the main effects of the pressure side flap



design parameters. At pre-stall, on average, drag is more sensitive to the flap deflection angle,  $\beta_p$  than the location  $x_p$  (figures 5(a) and (b)). Further, the response range, denoted by the red shaded region in figures 5(a) and (b), is narrow when the flap is near the leading edge or has a slight deflection angle. The narrow band indicates small control authority over the response in this area of the design space. For post-stall, the drag response is sensitive to both the flap location,  $x_p$ , and deflection angle,  $\beta_p$  (figures 5(e) and (f)). Unlike pre-stall, the post-stall range is significantly wider, with the maximum range observed near the trailing edge, where the drag coefficient varies from 0.2 to 1.2, indicating an order of magnitude increase in drag which allows more control authority over the response in the post-stall regime.

The drag response to the suction side flap design parameters is represented by the blue lines and shaded regions in figures 5(c), (d), (g) and (h). At pre-stall, drag decreases as the flap location changes from the leading edge towards the trailing edge, as indicated by the negative slope in figure 5(c). Drag also increases as the deflection angle,  $\beta_s$ , increases (figures 5(c) and (d)). At pre-stall, regardless of the specific flap configuration, the blue line is higher than the dashed baseline, indicating that the suction side covert flap increases drag. At post-stall angles of attack, on average, drag is mostly insensitive to the flap location and deflection angle, as indicated by the zero slope of the blue lines in figures 5(g) and (h). Moreover, unlike the pre-stall results, the average drag is less than the baseline configuration. Combining the lower post-stall drag with the previous observation of an average higher post-stall lift indicates that suction side flaps

can improve aerodynamic efficiency at post-stall conditions, confirming prior results about suction side covert-inspired flaps [14].

The simultaneous flap deflection results at pre-stall, indicated by the black lines and grey shaded region in figure 5, show that the drag coefficient is marginally sensitive to  $x_p$ . In contrast, changing the suction side flap location  $x_s$ , from the leading edge to the trailing edge decreases drag. While increasing both deflection angles increases drag, as indicated by the positive slopes in figures 5(b) and (d). At post-stall, drag is sensitive to the pressure side variables,  $x_p$ , and  $\beta_p$ , where an increase in the location or the deflection angle increases the drag. Suction side variables have zero slopes, hence changes in both  $x_s$ , and  $\beta_s$  do not change the average response of the simultaneously deployed flaps. Similar to the lift results, the simultaneous deflection increases the response range of drag. For example, in pre-stall, drag values range from matching the baseline values to a maximum of an 840% increase, while in post-stall, the drag response range includes flap configurations that can reduce the drag by 60% to other configurations that can increase drag by 200% compared to the baseline.

### 2.2.3. Pitching moment

The pitching moment completes the 2D picture of the system's response. Figure 6 shows the main effects of the flap parameters on the pitching moment, calculated at the quarter-chord of the airfoil. We first examine the effect of the pressure side flap, represented by the red lines and shaded regions in figures 6(a), (b), (e) and (f). At pre-stall, the quarter-chord pitching moment coefficient is sensitive to  $x_p$

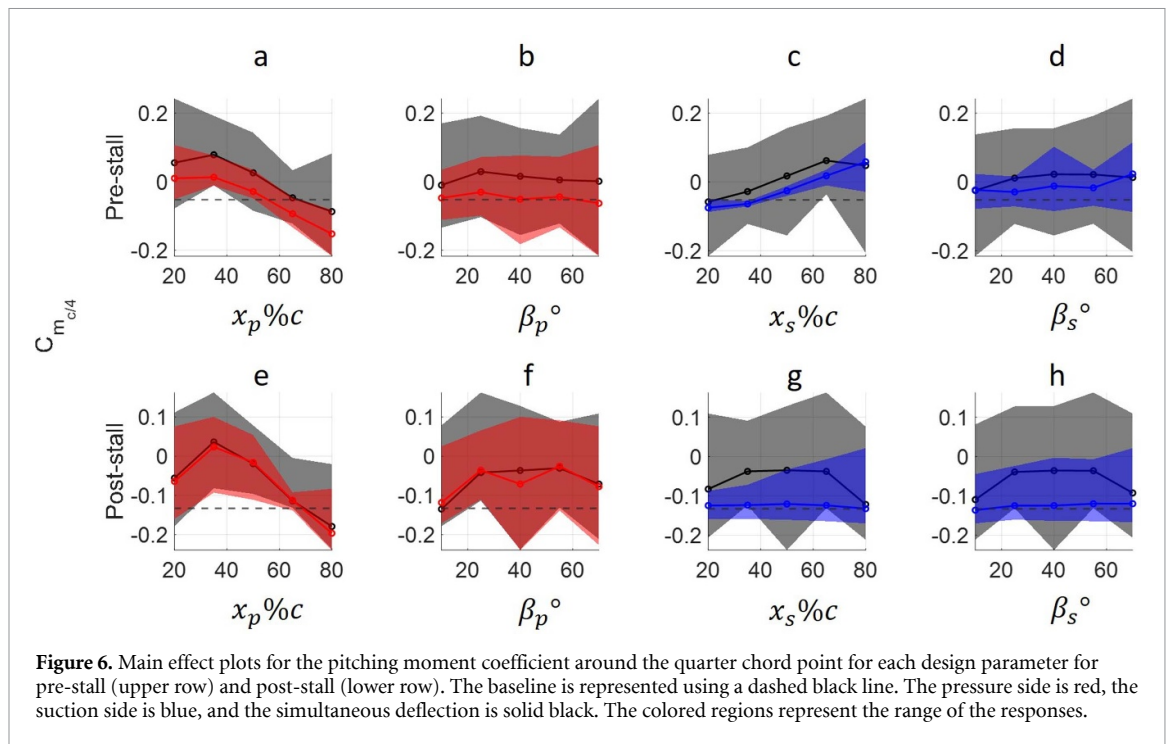


**Figure 6.** Main effect plots for the pitching moment coefficient around the quarter chord point for each design parameter for pre-stall (upper row) and post-stall (lower row). The baseline is represented using a dashed black line. The pressure side is red, the suction side is blue, and the simultaneous deflection is solid black. The colored regions represent the range of the responses.

(figure 6(a)). However, it is insensitive to  $\beta_p$  as indicated by the zero slope of the red line in figure 6(b). Moving the pressure side flap effectively changes the airfoil camber. For example, moving the pressure side flap towards the trailing edge increases the airfoil's effective camber, making  $C_m$  more negative. While moving the flap toward the leading edge decreases the effective camber, making  $C_m$  more positive. At post-stall, the pitching moment is still sensitive to  $x_p$ . However, unlike pre-stall, at post-stall, the pitching moment is slightly sensitive to  $\beta_p$ , where, by average, increasing the deflection angle  $\beta_p$ , increases  $C_m$ .

The pitching moment response to the suction side flap design parameters is represented by the blue lines and shaded regions in figures 6(c), (d), (g) and (h). At pre-stall, the pitching moment coefficient response is also a function of the location  $x_s$ ; however, the slope is opposite to the pressure side. In other words, deploying suction side flaps near the trailing edge has a decambering effect on the airfoil. Further, comparing the shaded regions in figures 6(a) and (c), the suction side range band is significantly smaller than the pressure side range band. Hence, the pressure side flap is more effective in modulating  $C_m$  compared to the suction side flap. Similar to the pressure side flap, the pitching moment is insensitive to the suction side deflection angle (figure 6(d)). At post-stall, the response has zero slopes in figures 6(g) and (h), indicating that, on average,  $C_m$  is insensitive to both  $x_s$ , and  $\beta_s$ . However, some configurations can produce pitching moments above or below the baseline, as represented by the shaded regions in figures 6(g) and (h).

The simultaneous deflection of the covert-inspired flap at pre-stall, indicated by the black lines in figure 6, shows that  $C_m$ , on average, is more sensitive to the location variables than the deflection angles. Moving the flaps from the leading edge towards the trailing edge on the pressure and suction sides increases and decreases the effective camber of the airfoil, respectively (figures 6(a) and (c)). Moreover, deflecting both the suction and pressure side flaps at pre-stall angles of attack allows for a wider range of modulating  $C_m$  as indicated by the area of the shaded grey regions compared to the shaded blue and red regions (figure 6). At post-stall, the pitching moment is mainly controlled by the pressure side location  $x_p$ . The other parameters have a zero slope in the middle of the design space and baseline values at the leading and trailing edges (figures 6(f), (g) and (h)). Similar to pre-stall, the black shaded regions show that the simultaneous deflection always has a broader range of response values compared to the pressure or suction sides alone.

#### 2.2.4. Aerodynamic characterization discussion

This section answers Q1 and Q2 posed in the introduction. For all the measured responses ( $C_l$ ,  $C_d$ , and  $C_m$ ), we show that the modulation range of simultaneously deflecting covert flaps is larger than one-sided deflections. Thus, one possible hypothesis for OBS 2 from Carruthers *et al* [5] is that birds deflect covert feathers on both sides simultaneously during flight to take advantage of the increased control range compared to the baseline or the one-sided flaps.



**Table 1.** Summary table of coverts control derivatives as approximate slopes of pressure and suction side variables for pre- and post-stall flight regimes.

	Pre-stall		Post-stall	
$C_l$	$\frac{\partial C_l}{\partial x_p} > 0$	$\frac{\partial C_l}{\partial x_s} \approx 0$	$\frac{\partial C_l}{\partial x_p} > 0$	$\frac{\partial C_l}{\partial x_s} \approx 0$
	$\frac{\partial C_l}{\partial \beta_p} \approx 0$	$\frac{\partial C_l}{\partial \beta_s} < 0$	$\frac{\partial C_l}{\partial \beta_p} \approx 0$	$\frac{\partial C_l}{\partial \beta_s} \approx 0$
$C_d$	$\frac{\partial C_d}{\partial x_p} \approx 0$	$\frac{\partial C_d}{\partial x_s} < 0$	$\frac{\partial C_d}{\partial x_p} > 0$	$\frac{\partial C_d}{\partial x_s} \approx 0$
	$\frac{\partial C_d}{\partial \beta_p} > 0$	$\frac{\partial C_d}{\partial \beta_s} > 0$	$\frac{\partial C_d}{\partial \beta_p} > 0$	$\frac{\partial C_d}{\partial \beta_s} \approx 0$
$C_m$	$\frac{\partial C_m}{\partial x_p} < 0$	$\frac{\partial C_m}{\partial x_s} > 0$	$\frac{\partial C_m}{\partial x_p} < 0$	$\frac{\partial C_m}{\partial x_s} \approx 0$
	$\frac{\partial C_m}{\partial \beta_p} \approx 0$	$\frac{\partial C_m}{\partial \beta_s} \approx 0$	$\frac{\partial C_m}{\partial \beta_p} \approx 0$	$\frac{\partial C_m}{\partial \beta_s} \approx 0$

Second, we explored Q2 to understand which parameters are most influential in the modulation of lift, drag, and pitching moment. Results show that flap design parameters can be effectively used as control knobs for the force and moment responses, with some knobs being more effective than others. For example, the pressure side location is the most effective knob as it can control lift, drag, and pitch moment in both the pre-stall and post-stall flow regimes. The deflection angles mainly control the drag response, and the interaction between  $x_p$  and  $x_s$  controls the effective camber of the airfoil. Table 1 shows the average control derivative sign for each response with respect to the experimental parameters for the pre-stall and post-stall AoA regimes. The sign of the control derivatives indicates whether the response had a direct (indicated by the +ve sign) or an inverse (indicated by the -ve sign) relationship with the experimental parameter. A zero control derivative suggests the response is insensitive to the experimental parameter.

The results discussed in this section support multiple observations from Carruthers *et al* [5]. We found that leading edge pressure flaps at post-stall cause a reduction in lift and increase the pitching moment, causing a pitch-up attitude change. This finding supports OBS 1 and provides a possible explanation of why birds deploy underwing lesser coverts in most landing and perching maneuvers. Additionally, OBS 3 states that greater upperwing coverts deflect during gusts. Gusts often increase the effective angle of attack and cause a sudden increase in lift. Thus, during gust encounters, it may be advantageous to reduce lift. Our results indicate that trailing edge suction side covert flaps, which are equivalent to the upperwing greater covert feathers, reduce lift at pre-stall, supporting OBS 3. Finally, OBS 4 states that birds deploy lesser underwing coverts at the end of a pitch-up maneuver. Our results show that a pressure side flap near the trailing edge, equivalent to lesser underwing coverts, decreases the pitching moment coefficient compared to the baseline, which would stop or slow down a pitch-up maneuver providing a possible

explanation of the timing of the lesser underwing covert deployment during birds' perching maneuvers.

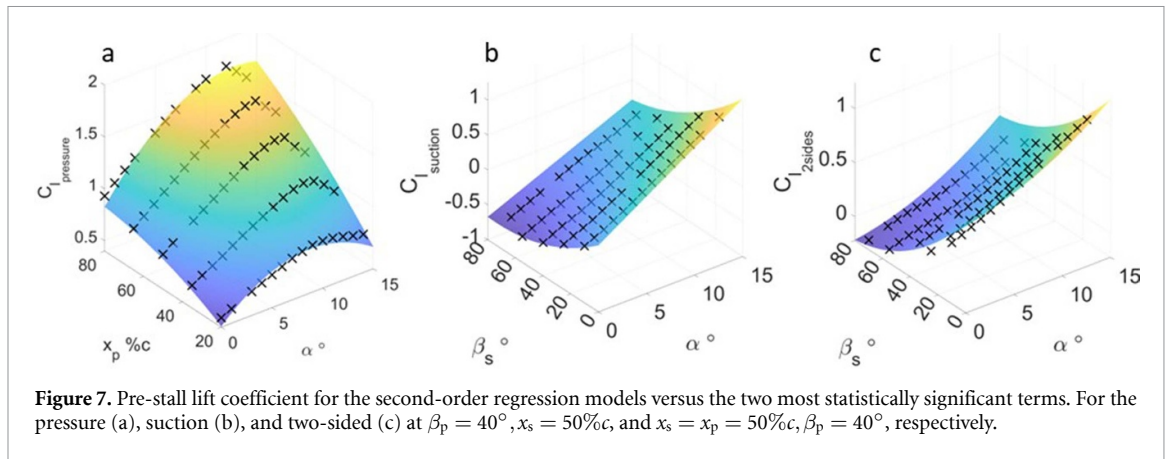
While the aerodynamic characterization answers Q1 and Q2, a more quantitative approach is needed to functionally relate the measured response to the experimental parameters. The following section presents data-driven models. These models can be used to quantify the interactions between the pressure side and suction side flaps, Q3, and identify the most significant parameters for controlling a given response, Q2. Such knowledge can also be applied as control laws for uncrewed aerial vehicles (UAVs) with covert-inspired flaps control effectors.

### 3. Data driven models

In this section, we derive aerodynamic models describing the response parameters ( $C_l$ ,  $C_d$ , and  $C_m$ ) as surface functions of the covert-flaps design parameters (i.e.  $x_p$ ,  $\beta_p$ ,  $x_s$ , and  $\beta_s$ ) and the flow parameter ( $\alpha$ ). These models serve two important functions. First, they identify the covert-inspired flap parameters most effective in modulating a given response (Q2). Second, the models determine the influence of interaction terms on the aerodynamic response (Q3). For example, they indicate whether simultaneous deflection of suction and pressure flaps have additive effects that can be modeled through the superposition of the one-sided flap models or if the interaction terms have a significant effect on the response and should be included explicitly in the model. Linear regression is used along with analysis of variance (ANOVA) analysis to generate and assess the quality of the aerodynamic models.

#### 3.1. Regression methods

Stepwise regression, a type of linear regression, was used to derive empirical models from quantitatively analyzing response trends. In stepwise regression, the model structure is changed and assessed while building the model. Hence, a good model can be found without excess terms or overfitting [23]. This paper used a minimum Bayesian Information Criterion



(min. BIC) as a stopping criterion for the stepwise regression based on the maximum likelihood function, which penalizes the addition of unnecessary terms in the model [23].

JMP Pro 16 was used for the regression and ANOVA analysis. Different flow regimes have different physical characteristics. Thus, the statistically significant parameters are different for each response and for each regime, and the analysis was, therefore, divided into pre- and post-stall for each response variable. For this two-dimensional study, the response variables were the coefficients of lift  $C_l$ , drag  $C_d$ , and pitching moment  $C_{m_{c/4}}$ . Each response was assumed to be affected by the variations in AoA,  $\alpha$ , and the covert-inspired flap's locations  $x_s$ ,  $x_p$  and deflection angles  $\beta_s$ ,  $\beta_p$ . A second-order response surface model was used to model all pre-stall responses. Each pre- and post-stall model was derived using only a 10% and 50% random sample of the total experimental data, respectively. The model was then validated using the remaining 90% and 50% of the data. All the validation points were in an independent data set that was not used for modeling. Maintaining a second-order model was preferred in this paper compared to higher-order models, even with relatively low  $R^2$ , to maintain the physical meaning and facilitate the understanding of the equations.

The significance of each term in the response models was checked using the  $P$ -value with a set significance level of 5%. The model quality was assessed using the coefficient of determination  $R^2$ , the adjusted coefficient of determination  $R_{adj}^2$ , and residual plots.  $R^2$  shows the improvement in the variation reduction of the modeled response versus the measured response due to the model, while the adjusted coefficient of determination  $R_{adj}^2$  penalizes adding non-significant terms to the model. Avoiding statistically insignificant terms can ensure that the model is not overfitted to a specific data set. Further, the residuals were plotted against the predicted and actual values to test for randomness, and the normal quantile plots were used to check for normality. More details

regarding the experimental design, linear regression, and ANOVA analysis can be found in [23, 27].

### 3.2. Model results

#### 3.2.1. Pre-stall

All models discussed here are shown in the [appendix](#). Each of the equations shown has units of degrees for all angles ( $10^\circ, 50^\circ, \dots$ ) and chord percent for the covert locations ( $20\%, 50\%, \dots$ ). The final units of the response are non-dimensional; hence to fix the units to match, the units are absorbed in the regression coefficients. The whole term (parameters and regressors), not only the regressors, have to be considered when comparing the contributions of different terms. The main effects terms,  $\alpha$ ,  $\beta_p$ , and  $x_p$ , along with the second order  $\alpha$  interaction terms are the most significant for the pre-stall lift model for the pressure side flap (equation (1)). In contrast, the pre-stall suction side flap model (equation (2)) shows that lift is driven by the angle of attack and the deflection angle  $\beta_s$ . Figure 7 shows the lift response surface for the pressure, suction, and simultaneous deflection experiments. The  $x$ - $y$  plane axes are each experiment's two most statistically significant parameters. The markers represent the measured values, while the response surface is the functional representation of the coefficient of the lift model. Figure 7 shows that the combined effect of the simultaneous deflection is most affected by  $\alpha$ ,  $x_p$ , and  $\beta_s$ , which supports the results from the main effects in figures 4(a) and (d). These models have  $R^2 = 85\%$  or more. Most of the error is near the boundaries, where there is a misalignment at the edges between the response surface and the measured data, most prominently shown in figure 7(a) at ( $x_p = 80\%c, \alpha = 15^\circ$ ). This discrepancy happens because the flap deployment reduces the stall angle when deployed at the trailing edge, which causes some interference between the pre- and post-stall regimes.

Pre-stall drag for each side alone is a function of the angle of attack  $\alpha$  and the corresponding deflection angles (equations (5) and (6)). The significance

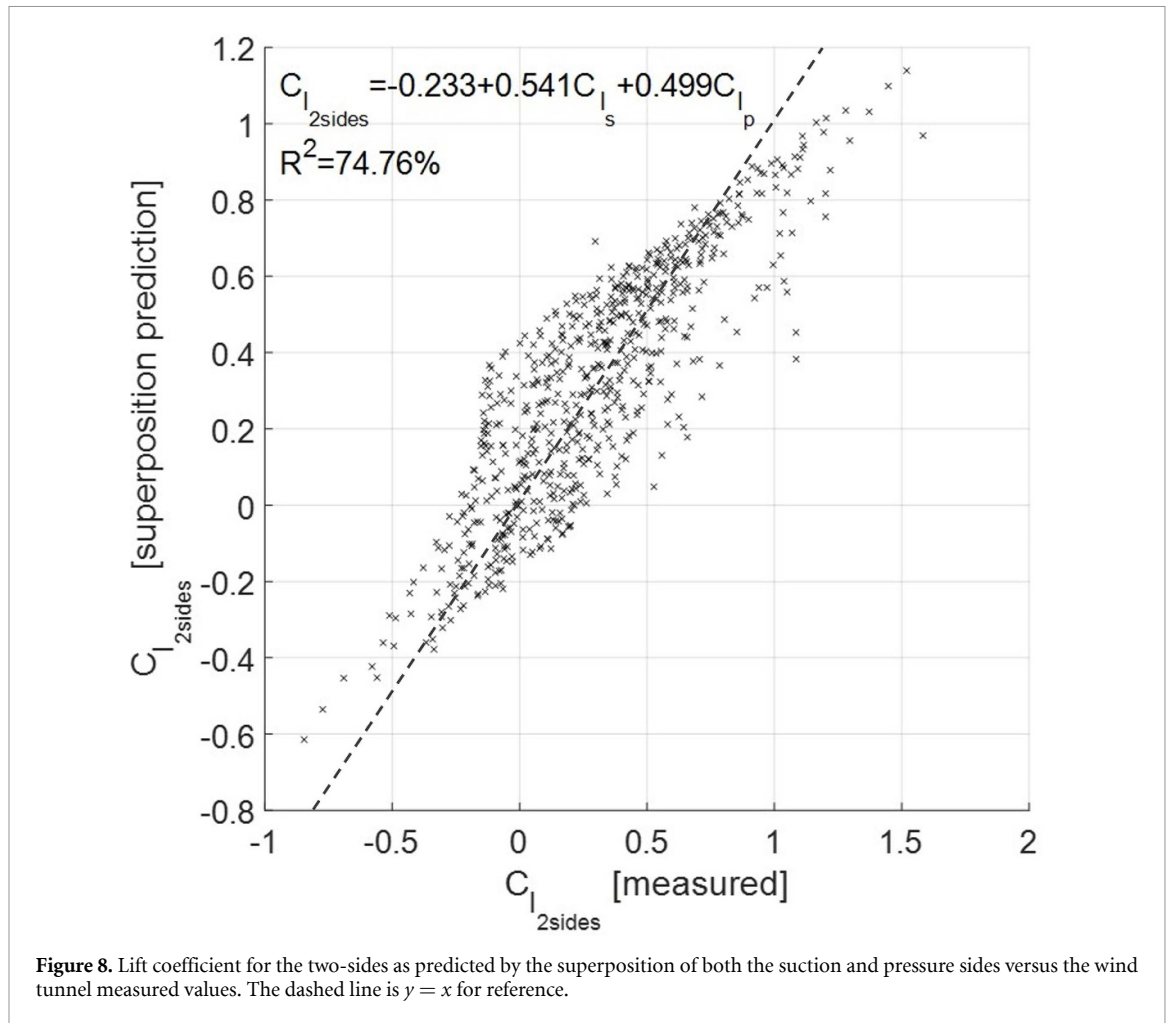


**Figure 8.** Lift coefficient for the two-sides as predicted by the superposition of both the suction and pressure sides versus the wind tunnel measured values. The dashed line is  $y = x$  for reference.

of the deflection angles is maintained for the simultaneous deflection experiment (equation (7)). As  $\beta_p$  and  $\beta_s$  increase, drag increases linearly. However, the model still has second-order interaction terms and quadratic terms. Unlike drag, pre-stall pitching moments are controlled mostly by the covert-flaps location (equations (9)–(11)).

The two-sided lift, drag, and pitching moment models (equations (3), (7) and (11)) include interaction terms. However, we also wanted to assess whether a similar response can be predicted by superimposing the models of the single flaps. Using the lift as an example, a linear regression approach was used to fit  $C_{l_{2sides}}$  in terms of  $C_{l_p}$  and  $C_{l_s}$ . The model is then plotted against the measured values for the simultaneous deflection experiment in figure 8. The figure shows that 75% of the simultaneous deflection response can be captured using only a linear combination of the suction and pressure responses (equation (4)). The remaining 25% are hypothesized to be emerging properties in the two-sided system, such as the interaction terms shown in the two-sided model (equation (3)), such as  $\beta_p\beta_s$ , and  $\beta_sx_p$ . Similarly, for drag, the interaction terms are significant and carry a lot of information; hence, a linear superposition of the drag's pressure and suction sides

models can only capture 67% of the two-sided experiment (equation (8)). Unlike lift and drag, the pre-stall pitching moment simultaneous deflection model can be predicted using the superposition principle with an  $R_{adj}^2 = 95.27$  (equation (12)).

### 3.2.2. Post-stall

At post-stall, for the pressure side flaps, the location is the main parameter for lift control, along with the interaction of the location and deflection angle ( $x_p\beta_p$ ) (equation (13)). For the suction side, the location,  $x_s$ , and the interaction term  $\alpha\beta_s$  are the most significant terms in the lift model (equation (14)). For the two-sided deflection, both pressure and suction terms are significant. However, the pressure terms are more prominent (equation (15)).

At post-stall, the drag model of the airfoil with the pressure side flap is a strong function of the angle of attack and the flap location rather than the deflection angles (equation (17)). For the suction side  $\alpha$  and  $\alpha x_s$  are the driving terms (equation (18)). The two-sided drag model has pressure side terms as leading terms (equation (19)), which supports results from previous sections (figures 5(e) and (f)). All drag models have a prediction power of more than 90%. Finally, the pressure side pitching moment model at post-stall

maintains its dependence on the pressure side flap location. However, the suction side's most significant term is the angle of attack (equations (21)–(23)).

Similar to the post-stall drag, the pitching moment two-sided deflection is mainly driven by the pressure side terms (figures 6(e) and (f)). Most of the suction side terms are statistically insignificant. At post-stall, the superposition holds well for all response variables, predicting more than 80% of the lift and pitching moment and 94% of the drag (equations (16), (20), and (24)).

### 3.2.3. Data-driven modeling discussion

This section derived the lift, drag, and pitching moment models for the airfoil with one- and two-sided covert-inspired flaps. The section also examined the validity of applying the superposition of the one-sided flap models to predict the two-sided response. The models show that at pre-stall, the lift is controlled by the angle of attack interactions with the suction side flaps, the drag is controlled by the deflection angles, and the flap locations control the pitching moment. At post-stall, the effect of the pressure side is more critical than the suction side, especially in the drag and pitching moment. Finally, we show that the superposition principle works sufficiently well as a predictor for all the post-stall responses and the pitching moment response for both regimes. In contrast, in the pre-stall regime, the interaction terms carry significant information for lift and drag.

## 4. Case study: covert-inspired flaps as yaw control devices

### 4.1. Problem setup

The previous sections discussed the sensitivities of the aerodynamic forces and moments to the covert-inspired flap system design parameters through main effects plots and data-driven models. This section presents a case study to showcase the selection process for a flap configuration to meet a desired performance metric. More specifically, we chose a case study of using the covert-inspired flaps as yaw control devices at a given trim condition. Thus, the objective of this case study is to choose a covert-inspired flaps configuration that maximizes drag and maintains lift with respect to a baseline configuration flying at a trim angle of attack of  $8^\circ$ . Maintaining lift is a critical requirement as it prevents undesirable rolling moments.

### 4.2. Choice of covert-inspired flap locations

Figures 9(a) and (b) are configuration choice plots, showing the experimentally measured lift and drag coefficients, respectively, at  $\alpha = 8^\circ$ . Each plot has the location parameters,  $x_p$  and  $x_s$ , plotted on the main  $x$

and  $y$  axes, respectively. Each inset plot has the deflection angles,  $\beta_p$ , and  $\beta_s$ , on its  $x$  and  $y$  axes. The percent improvement (or deficit) as compared to the baseline is represented by the color.

The change in lift at this angle of attack ranges between a 120% deficit to a 25% improvement depending on the location (figure 9(a)). It is also symmetric about  $x_s = 50\%c$ , with lift increasing as  $x_p$  moves toward the trailing edge. For every inset plot (configuration), lift increases as  $\beta_p$  increases and  $\beta_s$  decreases. A baseline matching value can be obtained for  $x_p = 80\%c$ . As for the drag (figure 9(b)), its range can be varied from baseline levels to an eight-times increase in magnitude. Drag increases as  $x_s$  moves from the trailing edge to the leading edge, and for a specific location configuration, it increases as both deflection angles increase. A maximum value of drag increase can be obtained at  $x_s = 20\%c$ . Combining both results, the suggested configuration to maximize drag and maintain lift, corresponding to modulating yaw while maintaining roll, is a pressure side flap located near the trailing edge and a suction side flap located near the leading edge (i.e.  $x_p = 80\%c$ ,  $x_s = 20\%c$ ).

A quantitative method of choosing the configuration can be applied by using JMP's prediction profiler, where the data-driven models are used with a cost function to produce an optimized response. We will again fix the trim condition at  $\alpha = 8^\circ$ . The objective cost functions are set to maximize the drag coefficient and match the baseline lift coefficient value. Given these objectives, the prediction profiler calculates a desired configuration of  $x_p = 80\%c$ ,  $\beta_p = 70^\circ$ ,  $x_s = 20\%c$ ,  $\beta_s = 54.5^\circ$ , which is similar to the configuration selected based on the experimental data plotted in figure 9. This configuration has the suction side flap located near the leading edge to drive the high drag response, mainly through the disruption of the suction peak. Moreover, the pressure side location is near the trailing edge because that is the most effective place to put a flap, according to the thin airfoil theory. This location gets the highest lift response, which counteracts the loss in lift due to the suction-peak reduction. As for the deflection angles, the final values are balanced such that the lift gains from the pressure side flap counteract the lift losses from the suction side flap.

At the optimal configuration, predicted by the profiler, the drag coefficient is maximized to a value of 0.59 compared to the baseline value of 0.07, which is more than eight times the baseline value. At that configuration, the lift is reduced from the baseline value of 0.91 to 0.58. This solution has the best desirability compared to other solutions in the parameter space. However, the baseline lift values can be matched with a larger area covert-inspired flap or allowing larger pressure side flap deflection angle. The former was



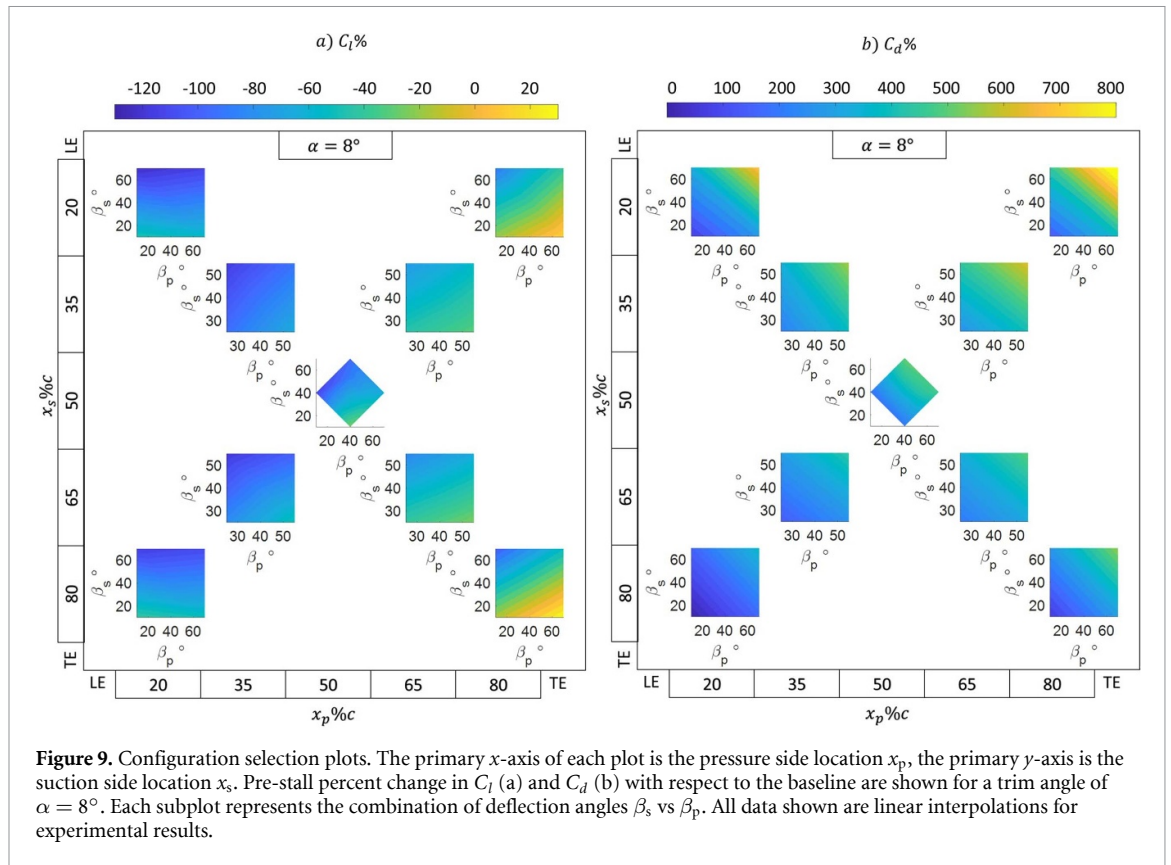


**Figure 9.** Configuration selection plots. The primary  $x$ -axis of each plot is the pressure side location  $x_p$ , the primary  $y$ -axis is the suction side location  $x_s$ . Pre-stall percent change in  $C_l$  (a) and  $C_d$  (b) with respect to the baseline are shown for a trim angle of  $\alpha = 8^\circ$ . Each subplot represents the combination of deflection angles  $\beta_s$  vs  $\beta_p$ . All data shown are linear interpolations for experimental results.

tested in another experiment and showed matching values for the lift.

## 5. Conclusion

Inspired by observations of the covert feather deployment during bird flight, we designed a covert-inspired flap system to investigate the effect of deploying covert-inspired flaps on the suction side, pressure side, and both sides of a wing section. We varied the flaps' chord-wise location, deflection angle, and the wing's angle of attack. The study answers three main questions related to the simultaneous deflection of suction side and pressure side flaps. More specifically, the study answers the following questions:

**Q1** What is the effect of the simultaneous static deflection of pressure and suction covert-inspired flaps on the aerodynamic forces and moments compared to a single-sided flap alone?

**Ans:** Results show that the simultaneous deflection of suction and pressure side flaps is more analogous to the behavior observed in nature. Simultaneously deflecting flaps on an airfoil's suction and pressure sides produces a broader control range over the aerodynamic forces and moments compared to a one-sided flap alone.

**Q2** Which flap parameters are most effective at modulating the aerodynamic forces and moments?

**Ans:** In general, the lift force changes are most sensitive to the location of the pressure side flap and the deflection angle of the suction side flap. Drag is most sensitive to the pressure side deflection angle. The flaps generally increase drag pre-stall, but some flap configurations decrease drag at post-stall angles of attack. The pitching moment results show that the suction side flap has a de-cambering effect, while the pressure side flap effectively increases the camber. The pitching moment is more sensitive to the pressure side flap than the suction side flap and more sensitive to location changes than the deflection angle changes.

**Q3** What are the interactions between the suction and pressure side covert-inspired flaps, are the flap effects purely additive, or do interactions between both flaps govern the aerodynamic response?

**Ans:** One of the article's contributions involved deriving data-driven models to relate the flap design parameters to the aerodynamic response quantitatively. The models confirmed the finding of the wind tunnel results, identifying the most significant flap parameters for a given response. The data-driven models also indicate significant interactions between the suction and pressure side flaps, especially during the pre-stall regime



for the lift and drag response, such that these responses cannot be fully predicted by simply superimposing the one-sided flap models.

The findings of this paper are relevant in providing insights into the role of covert feathers during bird flight. For example, our results indicate that simultaneously deploying suction and pressure side coverts allow for a broader range of modulating the aerodynamic forces and moments. Thus, the simultaneous deployment of covert feathers in nature can suggest that both suction and pressure side coverts enable birds to repeatedly perform various maneuvers, such as landing, gliding, and perching. In addition to formulating new hypotheses about the coverts role in bird flight, the current study can be utilized to develop a framework to design covert-inspired flow and flight control systems for UAVs operating similar Reynolds number regimes. The case study presented in the article shows the feasibility of using covert-inspired flaps as yaw control devices. This study is the first step in developing a complete framework for active bio-inspired flight control devices. Future work includes wider variations in the design parameter space and dynamic characterization of the covert-inspired flaps.

### Data availability statement

The data used in the manuscript is part of an ongoing collaboration with an industry project. However, we can easily accommodate data requests. The data that support the findings of this study are available upon reasonable request from the authors.

### Acknowledgments

The authors would like to acknowledge funding from The Toyota Research Institute of North America and the National Science Foundation (Award No. 2029028). Moreover, certain images in this publication have been obtained by the author(s) from the Pixabay website, where they were made available under the Pixabay License. To the extent that the law allows, IOP Publishing disclaims any liability that any person may suffer as a result of accessing, using or forwarding the image(s). Any reuse rights should be checked and permission should be sought, if necessary, from Pixabay and/or the copyright owner (as appropriate) before using or forwarding the image(s).

### Appendix

$$\begin{aligned} preC_{l_p} &= -0.514 + [-544.0\alpha^2 - 44.6\alpha\beta_p + 71.0\alpha x_p \\ &\quad + 9880.0\alpha - 15.6\beta_p^2 \\ &\quad + 2250.0\beta_p - 8.07x_p^2 + 1510.0x_p] \times 10^{-5} \\ R_{adj,model}^2 &= 98.79\% - R_{adj,validation}^2 = 86.87\% \end{aligned} \quad (1)$$

$$\begin{aligned} preC_{l_s} &= 0.0967 + [5540.0\alpha - 1530.0\beta_s - 286.0x_s \\ &\quad - 34.9\alpha\beta_s + 63.3\alpha x_s - 3.97\beta_s x_s \\ &\quad + 11.8\beta_s^2] \times 10^{-5} \\ R_{adj,model}^2 &= 99.59\% - R_{adj,validation}^2 = 98.56\% \end{aligned} \quad (2)$$

$$\begin{aligned} preC_{l_{2sides}} &= 0.273 + [578.0\beta_p - 3980.0\alpha - 1330.0\beta_s \\ &\quad + 420.0x_p - 584.0x_s - 37.1\alpha\beta_p + 54.7\alpha x_p \\ &\quad + 81.3\alpha x_s - 5.22\beta_p\beta_s + 9.1\beta_p x_p - 6.8\beta_s x_p \\ &\quad + 195.0\alpha^2 + 10.7\beta_s^2] \times 10^{-5} \\ R_{adj,model}^2 &= 95.11\% - R_{adj,validation}^2 = 90.36\% \end{aligned} \quad (3)$$

$$\begin{aligned} preC_{l_{2sides}} &= -0.233 + 0.541C_{l_s} + 0.499C_{l_p} \\ R_{adj,model}^2 &= 72.75\% - R_{adj,validation}^2 = 74.76\% \end{aligned} \quad (4)$$

$$\begin{aligned} preC_{d_p} &= 0.00673 + [32.5\alpha^2 + 14.6\alpha x_p - 645.0\alpha \\ &\quad - 1.0\beta_p^2 + 323.0\beta_p - 1.28x_p^2 + 98.8x_p] \times 10^{-5} \\ R_{adj,model}^2 &= 97.89\% - R_{adj,validation}^2 = 95.73\% \end{aligned} \quad (5)$$

$$\begin{aligned} preC_{d_s} &= 0.02760 + [541.0\alpha + 332.0\beta_s + 23.0x_s - 8.55\alpha x_s \\ &\quad - 1.61\beta_s x_s + 27.1\alpha^2] \times 10^{-5} \\ R_{adj,model}^2 &= 98.16\% - R_{adj,validation}^2 = 98.07\% \end{aligned} \quad (6)$$

$$\begin{aligned} preC_{d_{2sides}} &= -0.144 + [1010.0\alpha + 426.0\beta_p + 689.0\beta_s \\ &\quad + 256.0x_p + 79.7x_s - 10.2\alpha\beta_p - 8.14\alpha\beta_s \\ &\quad + 14.5\alpha x_p - 16.2\alpha x_s + 1.64\beta_p\beta_s - 1.71\beta_p x_s \\ &\quad - 2.47\beta_s x_s - 2.66\beta_s^2 - 2.33x_p^2 + 0.322x_s^2] \times 10^{-5} \\ R_{adj,model}^2 &= 96.55\% - R_{adj,validation}^2 = 94.44\% \end{aligned} \quad (7)$$

$$\begin{aligned} preC_{d_{2sides}} &= 0.0103 + 1.15C_{d_s} + 0.729C_{d_p} \\ R_{adj}^2 &= 67.82\% \end{aligned} \quad (8)$$

$$\begin{aligned} preC_{m_p} &= 0.0482 + [66.3\alpha^2 - 10.4\alpha x_p - 82.0\alpha \\ &\quad + 2.23\beta_p^2 - 1.32\beta_p x_p - 181.0\beta_p \\ &\quad - 3.09x_p^2 + 102.0x_p] \times 10^{-5} \\ R_{adj,model}^2 &= 98.14\% - R_{adj,validation}^2 = 82.16\% \end{aligned} \quad (9)$$

$$\begin{aligned} preC_{m_s} &= -0.0998 + [281.0\alpha - 35.6\beta_s + 22.4x_s \\ &\quad - 8.16\alpha x_s + 4.24\beta_s x_s - 1.78\beta_s^2 \\ &\quad + 1.4x_s^2] \times 10^{-5} \\ R_{adj,model}^2 &= 98.36\% - R_{adj,validation}^2 = 92.97\% \end{aligned} \quad (10)$$

$$\begin{aligned} preC_{m_{2sides}} &= -0.0182 + [1540.0\alpha + 27.2\beta_p - 50.9\beta_s \\ &\quad + 81.0x_p - 38.5x_s - 8.73\alpha x_p - 5.27\alpha x_s \\ &\quad - 3.82\beta_p x_p + 2.28\beta_p x_s + 2.1\beta_s x_s \\ &\quad + 2.57x_p x_s - 42.0\alpha^2 - 3.15x_p^2] \times 10^{-5} \\ R_{adj,model}^2 &= 89.95\% - R_{adj,validation}^2 = 84.09\% \end{aligned} \quad (11)$$

$$\begin{aligned} preC_{m_{2sides}} &= 0.0821 + 1.06C_{m_s} + 1.11C_{m_p} \\ R_{adj}^2 &= 95.27\% \end{aligned} \quad (15)$$

$$\begin{aligned} postC_{l_p} &= 2.18 + [20.5\beta_p x_p - 1290.0\beta_p - 553.0x_p \\ &\quad - 26.7\alpha x_p - 11400\alpha + 258.0\alpha^2 + 12.5x_p^2]10^{-5} \\ R_{adj_{model}}^2 &= 86.86\% - R_{adj_{validation}}^2 = 81.33\% \end{aligned} \quad (13)$$

$$\begin{aligned} postC_{l_s} &= 0.0282 + [4490.0\alpha - 2090.0\beta_s + 1170.0x_s \\ &\quad + 70.3\alpha\beta_s - 49.6\alpha x_s \\ &\quad + 5.42\beta_s x_s - 86.4\alpha^2] \times 10^{-5} \\ R_{adj_{model}}^2 &= 74.30\% - R_{adj_{validation}}^2 = 65.74\% \end{aligned} \quad (14)$$

$$\begin{aligned} postC_{l_{2sides}} &= 1.05 + [156.0x_p - 1190.0\beta_p - 1110.0\beta_s \\ &\quad - 2840.0\alpha + 493.0x_s + 33.9\alpha\beta_s - 34.5\alpha x_p \\ &\quad - 24.9\alpha x_s + 17.7\beta_p x_p + 4.82\beta_s x_s \\ &\quad + 93.5\alpha^2 + 8.4x_p^2] \times 10^{-5} \\ R_{adj_{model}}^2 &= 83.93\% - R_{adj_{validation}}^2 = 80.16\% \end{aligned} \quad (15)$$

$$\begin{aligned} postC_{l_{2sides}} &= -0.371 + 0.555C_{l_s} + 0.893C_{l_p} \\ R_{adj}^2 &= 86.97\% \end{aligned} \quad (16)$$

$$\begin{aligned} postC_{d_p} &= 0.120 + [1570.0\alpha - 137.0\beta_p - 979.0x_p \\ &\quad + 24.9\alpha x_p + 9.99\beta_p x_p \\ &\quad + 5.21x_p^2] \times 10^{-5} \\ R_{adj_{model}}^2 &= 93.66\% - R_{adj_{validation}}^2 = 91.67\% \end{aligned} \quad (17)$$

$$\begin{aligned} postC_{d_s} &= -0.106 + [2440.0\alpha + 222.0\beta_s - 395.0x_s \\ &\quad - 9.27\alpha\beta_s + 13.2\alpha x_s \\ &\quad + 1.09x_s^2] \times 10^{-5} \\ R_{adj_{model}}^2 &= 96.79\% - R_{adj_{validation}}^2 = 96.30\% \end{aligned} \quad (18)$$

$$\begin{aligned} postC_{d_{2sides}} &= 0.489 + [320.0\beta_s - 90.8\beta_p - 1620.0\alpha \\ &\quad - 886.0x_p - 203.0x_s - 11.0\alpha\beta_s \\ &\quad + 17.8\alpha x_p + 9.53\alpha x_s + 7.88\beta_p x_p \\ &\quad - 1.19\beta_s x_s + 67.0\alpha^2 \\ &\quad + 6.51x_p^2] \times 10^{-5} \\ R_{adj_{model}}^2 &= 93.36\% - R_{adj_{validation}}^2 = 92.83\% \end{aligned} \quad (19)$$

$$\begin{aligned} postC_{d_{2sides}} &= 0.0395 + 0.0831C_{d_s} + 0.868C_{d_p} \\ R_{adj}^2 &= 94.82\% \end{aligned} \quad (20)$$


$$\begin{aligned} postC_{m_p} &= -0.107 + [384.0\beta_p - 1090.0\alpha + 903.0x_p \\ &\quad + 15.5\alpha x_p - 6.39\beta_p x_p - 12.6x_p^2] \times 10^{-5} \\ R_{adj_{model}}^2 &= 86.34\% - R_{adj_{validation}}^2 = 80.97\% \end{aligned} \quad (21)$$

$$\begin{aligned} postC_{m_s} &= 0.227 + [158.0\beta_s - 3060.0\alpha + 99.5x_s \\ &\quad - 5.88\alpha\beta_s + 59.7\alpha^2 - 1.2x_s^2] \times 10^{-5} \\ R_{adj_{model}}^2 &= 74.70\% - R_{adj_{validation}}^2 = 76.56\% \end{aligned} \quad (22)$$

$$\begin{aligned} postC_{m_{2sides}} &= -0.0737 + [335.0\beta_p - 1030.0\alpha + 780.0x_p \\ &\quad + 14.7\alpha x_p - 5.38\beta_p x_p - 11.7x_p^2] \times 10^{-5} \\ R_{adj_{model}}^2 &= 80.96\% - R_{adj_{validation}}^2 = 80.90\% \end{aligned} \quad (23)$$

$$\begin{aligned} postC_{m_{2sides}} &= 0.0202 + 0.174C_{m_s} + 0.954C_{m_p} \\ R_{adj}^2 &= 93.20\% \end{aligned} \quad (24)$$

## ORCID iDs

Diaa A Zekry  <https://orcid.org/0000-0001-5851-1506>

Aimy A Wissa  <https://orcid.org/0000-0002-8468-511X>

## References

- [1] March A I, Bradley C W and Garcia E 2005 Aerodynamic properties of avian flight as a function of wing shape *ASME Int. Mechanical Engineering Congress and Exposition* vol 42193 pp 955–63
- [2] Thomas A L 1993 On the aerodynamics of birds' tails *Phil. Trans. R. Soc. B* **340** 361–80
- [3] Dvořák R 2016 Aerodynamics of bird flight *EPJ Web Conf.* **114** 01001
- [4] Guzmán M, Páez C R, Maldonado F J, Zufferey R, Tormo-Barbero J, Acosta JA and Ollero A 2021 Design and comparison of tails for bird-scale flapping-wing robots 2021 *IEEE/RSJ Int. Conf. on Intelligent Robots and Systems (IROS)* (IEEE) pp 6358–65
- [5] Carruthers A C, Thomas A L and Taylor G K 2007 Automatic aeroelastic devices in the wings of a steppe eagle *Aquila nipalensis* *J. Exp. Biol.* **210** 4136–49
- [6] Harvey C, Baliga V, Wong J, Altshuler D and Inman D 2022 Birds can transition between stable and unstable states via wing morphing *Nature* **603** 648–53
- [7] Videler J J 2006 *Avian Flight* (Oxford: Oxford University Press)
- [8] Brown R, Ferguson J, Lawrence M and Lees D 1987 *Tracks and Signs of the Birds of Britain and Europe: Christopher Helm* (London: Bloomsbury Publishing)
- [9] Duan C and Wissa A 2021 Covert-inspired flaps for lift enhancement and stall mitigation *Bioinspir. Biomim.* **16** 046020
- [10] Meyer R, Hage W, Bechert D W, Schatz M, Knacke T and Thiele F 2007 Separation control by self-activated movable flaps *AIAA J.* **45** 191–9
- [11] Bechert D, Bruse M, Hage W, Meyer R, Bechert D, Bruse M, Hage W and Meyer R 1997 Biological surfaces and their technological application-laboratory and flight experiments on drag reduction and separation control *28th Fluid Dynamics Conf.* p 1960
- [12] Bechert D, Bruse M, Hage W and Meyer R 2000 Fluid mechanics of biological surfaces and their technological application *Naturwissenschaften* **87** 157–71
- [13] Brücker C and Weidner C 2014 Influence of self-adaptive hairy flaps on the stall delay of an airfoil in ramp-up motion *J. Fluids Struct.* **47** 31–40
- [14] Duan C, Waite J and Wissa A 2018 Design optimization of a covert feather-inspired deployable structure for increased lift *2018 Applied Aerodynamics Conf.* p 3174

- [15] Gardner A, Opitz S, Wolf C and Merz C B 2017 Reduction of dynamic stall using a back-flow flap *CEAS Aeronaut. J.* **8** 271–86
- [16] Wang L, Alam M M and Zhou Y 2019 Experimental study of a passive control of airfoil lift using bioinspired feather flap *Bioinspir. Biomim.* **14** 066005
- [17] Fang Z, Gong C, Revell A, Chen G, Harwood A and O'Connor J 2019 Passive separation control of a NACA0012 airfoil via a flexible flap *Phys. Fluids* **31** 101904
- [18] Nair N J and Goza A 2022 Fluid-structure interaction of a bio-inspired passively deployable flap for lift enhancement (arXiv:2203.00037)
- [19] Barlow J B, Rae W H and Pope A 1999 *Low-Speed Wind Tunnel Testing* (New York: Wiley)
- [20] Etkin B and Reid L D 1959 *Dynamics of Flight* vol 2 (New York: Wiley)
- [21] Zekry D A, Duan C, Ito M R and Wissa A A 2021 Design of experiments for two- and three-dimensional bio-inspired flow control devices *AIAA Scitech 2021 Forum* p 0467
- [22] Montgomery D 2001 *Design and Analysis of Experiments* 5th edn (New York: Wiley)
- [23] Montgomery D C 2013 *Montgomery Design and Analysis of Experiments* vol 2009 8th edn (Hoboken, NJ: Arizona state university) p 2001
- [24] Landman D, Simpson J, Mariani R, Ortiz F and Britcher C 2007 Hybrid design for aircraft wind-tunnel testing using response surface methodologies *J. Aircr.* **44** 1214–21
- [25] DeLoach R 1998 Applications of modern experiment design to wind tunnel testing at NASA Langley research center *36th AIAA Aerospace Sciences Meeting and Exhibit* p 713
- [26] Othman A K, Nair N J, Sandeep A, Goza A and Wissa A 2022 *Numerical and experimental study of a covert-inspired passively deployable flap for aerodynamic lift enhancement AIAA AVIATION 2022 Forum* (American Institute of Aeronautics and Astronautics Inc)
- [27] Bogartz R S 1994 *An Introduction to the Analysis of Variance* (Goleta, CA: Praeger Publishers)